

Effect of external fields in high Chern number quantum anomalous Hall insulators

Yuriko Baba ^{1,*} Mario Amado ² Enrique Diez ² Francisco Domínguez-Adame ¹ and Rafael A. Molina ³

¹*Grupo Interdisciplinar de Sistemas Complejos (GISC), Departamento de Física de Materiales, Universidad Complutense, E-28040 Madrid, Spain*

²*Nanotechnology Group, USAL-Nanolab, Universidad de Salamanca, E-37008 Salamanca, Spain*

³*Instituto de Estructura de la Materia, IEM-CSIC, E-28006 Madrid, Spain*



(Received 11 September 2022; accepted 22 November 2022; published 19 December 2022)

A quantum anomalous Hall state with a high Chern number has so far been realized in multilayer structures consisting of alternating magnetic and undoped topological insulator (TI) layers. However, in previous proposals, the Chern number can only be tuned by varying the doping concentration or the width of the magnetic TI layers. This drawback largely restricts the applications of dissipationless chiral edge currents in electronics since the number of conducting channels remains fixed. In this paper, we propose a way of varying the Chern number at will in these multilayered structures by means of an external electric field applied along the stacking direction. In the presence of an electric field in the stacking direction, the inverted bands of the unbiased structure coalesce and hybridize, generating new inverted bands and collapsing the previously inverted ones. In this way, the number of Chern states can be tuned externally in the sample, without the need for modifying the number and width of the layers or the doping level. We showed that this effect can be uncovered by the variation of the transverse conductance as a function of the electric field at constant injection energy at the Fermi level.

DOI: [10.1103/PhysRevB.106.245305](https://doi.org/10.1103/PhysRevB.106.245305)

I. INTRODUCTION

Topological materials show great promise for future applications in electronics. The various members of the family of topological materials manifest a wide range of interesting properties, but the most significant one is dissipationless electric transport through the chiral edge or surface states. The introduction of the resistance standard based on the quantum Hall effect is a salient example of the applications of topological properties of materials, as it was a groundbreaking advance in metrology [1].

The family of quantum Hall effects now includes the quantum spin Hall effect [2] and the quantum anomalous Hall effect [3]. These effects do not require an external magnetic field to occur, and the main difference between them is the presence or absence of time-reversal symmetry. While the classical anomalous Hall effect was discovered in ferromagnetic materials by Hall himself [4], its quantum counterpart was the last of the family of quantum Hall effects to be measured, and this happened only recently. Early experiments used magnetically doped topological insulator (TI) thin films [5], where the magnetic impurities provided the breaking of time-reversal symmetry needed to observe the anomalous Hall effect.

A recent development of the quantum anomalous Hall effect has been achieved in heterostructures made of TI layers with and without magnetic doping. Depending on the number of layers, the Chern number C , the topological quantity measuring the number of edge states, can be controlled at will

[6,7]. Chern numbers as high as $C = 5$ have been measured in experiments using this technique [8].

On the other hand, external electromagnetic fields can be used to manipulate the topological properties of materials. In fact, dc electric fields can induce a topological phase transition depending on their strength in TIs [9,10] as well as in topological semimetals [11,12]. Application of external electric fields can renormalize the Fermi velocity and control the spatial decay of the surface states in Dirac materials [13–15]. Time-dependent electromagnetic fields can also be used for controlling topological properties of matter [16–24]. These studies have also been extended to magnetic TIs, showing clear signatures of the quantum anomalous Hall effect [25,26].

In the case of high Chern number magnetic insulators, it would certainly be desirable to tune the topological properties in the same sample by means of electric fields. In fact, an external electric field could be of use in different types of electronic devices where a fast change in the amount of current or the effective electrical resistance are needed. The goal of this paper is to study the effect of an electric field in the topological properties of heterostructures with magnetic doping showing the anomalous Hall effect with high Chern numbers. We will focus on the experimentally feasible heterostructures made of Bi_2Se_3 with layers with Cr doping. We will present Chern number maps as a function of the heterostructure parameters and different values of the electric field. These maps display a rich structure, allowing us to fine-tune the values of the Chern number, the number of edge states, and consequently, the transport properties of the device. We have also studied the evolution of the spatial localization of the electron states along the stacking and transverse directions as a function of the electrical field to have a deeper understanding of how Chern number changes take place.

*yuribaba@ucm.es

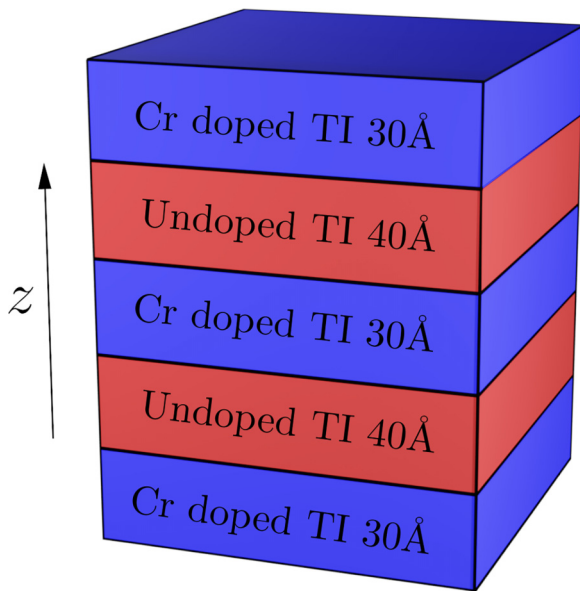


FIG. 1. Schematic representation along the stacking direction z of alternated Cr^- -doped (30 Å) and undoped films (40 Å) of the topological insulator (TI) heterostructure.

II. MODEL

The system under consideration consists of alternated magnetically doped and undoped layers of the same TI, as depicted in Fig. 1. To study the electron states in the TI, we use the low-energy Hamiltonian introduced in Ref. [27]. We write it in the basis of the bands of bonding and antibonding p_z orbitals ordered as $|P_1^+ \uparrow\rangle$, $|P_2^- \downarrow\rangle$, $|P_1^+ \downarrow\rangle$, $|P_2^- \uparrow\rangle$, where the superscripts \pm stand for even and odd parity, and \uparrow , \downarrow represent spin-up and spin-down states, respectively. In this basis, the Hamiltonian reads

$$\mathcal{H}(z, \mathbf{k}_{\parallel}) = \begin{bmatrix} H_+(z, \mathbf{k}_{\parallel}) & Bk_z \sigma_y \\ Bk_z \sigma_y & H_-(z, \mathbf{k}_{\parallel}) \end{bmatrix}, \quad (1)$$

where $H_{\pm}(\mathbf{k})$ describes two blocks of 2×2 models with opposite chiralities, hybridized by the terms proportional to B , which are linear in k_z . The H_{\pm} are given by the following expression:

$$H_{\pm}(z, \mathbf{k}_{\parallel}) = \epsilon(\mathbf{k}_{\parallel}, z) \mathbb{1}_2 + [M(z, \mathbf{k}_{\parallel}) \mp g(z)] \tau_3 + Ak_x \tau_1 \pm Ak_y \tau_2, \quad (2)$$

with $g(z)$ being the Zeeman splitting at position z along the stacking direction and $\mathbb{1}_n$ the $n \times n$ unit matrix. In Eqs. (1) and (2), σ_i and τ_i denote Pauli matrices acting in the spin basis and the basis of P_1^+ and P_2^- subbands, respectively. The onsite term and the mass term are respectively given by $\epsilon(z, \mathbf{k}_{\parallel}) = C_0 - C_1 \partial_z^2 + C_2(k_x^2 + k_y^2)$ and $M(z, \mathbf{k}) = M_0(z) - M_1 \partial_z^2 + M_2(k_x^2 + k_y^2)$. The topology of the Hamiltonian is given by the sign of the mass parameters: if $M_0 < 0$ and $M_1, M_2 > 0$, the system is in the inverted regime. On the other hand, the diagonal term $\epsilon(z, \mathbf{k}_{\parallel})$ accounts for the particle-hole asymmetry and has no impact on the topological nature of the bands. Therefore, $\epsilon(z, \mathbf{k}_{\parallel})$ can be set to zero without loss of generality.

Due to the Cr^- magnetic doping, a Zeeman splitting is induced in the magnetic region [28], and the band inversion tends to reduce [29]. Therefore, the mass $M_0(z)$ and the Zeeman splitting $g(z)$ parameters of the heterostructure are modeled by steplike functions along the stacking direction, following the same dependence as in Ref. [8]. In the undoped region, $g(z) = 0$, and the mass term takes the pristine value $M_0(z) = M_0$. In the Cr^- doped region, $M_0(z) = M_0^{\text{Cr}}$, and $g(z) = g$, where both values are tuned by the doping concentration. Notice that $g > 0$, and in Eq. (1), we set the splitting to be equal in both orbitals but opposite signs depending on the spin.

Finally, an external electric field is added as a linear potential in the stacking direction given by

$$\mathcal{H}_f = efz \mathbb{1}_4, \quad (3)$$

where e is the elementary electric charge, and f is the external electric field.

III. RESULTS

For concreteness, we focus on the heterostructure reported in Ref. [8] and shown schematically in Fig. 1. The layered structure under consideration consists of three films of three quintuple layers (3QL) of $(\text{Bi}, \text{Sb})_{2-x}\text{Cr}_x\text{Te}_3$ with two films of four quintuple layers (4QL) of $(\text{Bi}, \text{Sb})_2\text{Te}_3$ in between. In the following, we will refer to the Cr^- -doped 3QL as Cr^- QL and to the pristine TI 4QL as TI-QL, whose widths are 30 and 40 Å, respectively.

This configuration is highly symmetric and enables access to high Chern number (C) states up to 4 in the absence of an electric field. As shown in Fig. 2(a), the phase diagram of the system comprises wide regions where $C = 1, 2$, and 4 and a small region with $C = 3$. Notice that the region with $C = 4$ is inconsistent with the results presented in Ref. [8], as already pointed out by Wang and Li [30]. However, we find that a small region with $C = 3$ is present in between those with $C = 2$ and 4, in contrast to Ref. [30]. The inversion symmetry in the z direction assures that the states come in pairs, except in the case of the fully interlayer-connected $C = 1$ state; due to the finite-sized effect and the subsequent discretization of levels, the $C = 3$ region pops out in tight-binding models. In the results shown, the parameters correspond to the binary compound Bi_2Te_3 described in Ref. [27]. As already proved in Ref. [8] by computing the phase maps for Sb_2Te_3 , no qualitative modifications are expected in the case of the Sb binary compound or the ternary compound that resembles the experimental reference.

Notice that the phase diagrams are plotted as a function of both g and M_0^{Cr} as independent parameters. However, the doping concentration is expected to modify both quantities [28,29] in a correlated way. Therefore, the complete phase diagram is not accessible experimentally if multiple samples must be grown to modify the doping concentration and the Chern number. Due to this issue, an external field that dynamically changes the properties of a given device is a remarkable alternative to tuning the Chern number. More precisely, an electric field in the direction of growth does not break the translation symmetry of the system in x and y directions, enabling the Chern number to be computed in an effective

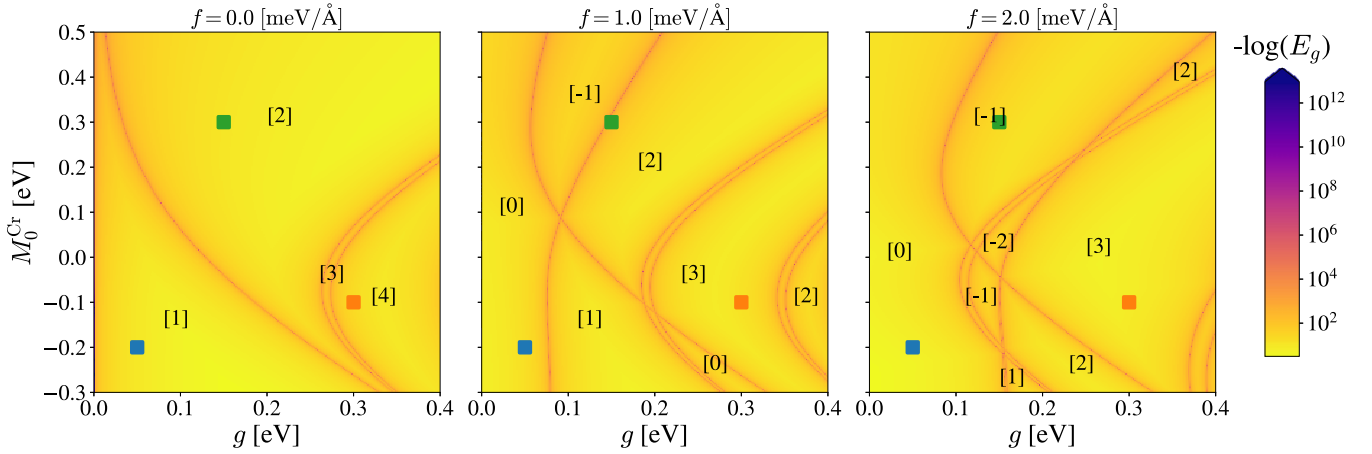


FIG. 2. Phase diagram of the energy gap (expressed in eV), in logarithmic scale, and the Chern numbers of the system indicated between the regions of gap closing. Electric fields of (a) 0 meV/Å, (b) 1 meV/Å, and (c) 2 meV/Å. The blue, orange, and green squares correspond to the calculated points in Fig. 8.

two-dimensional (2D) quantum Hall insulator. In Fig. 2, we plot the evolution of the gap phase map with the electric field. We use the method implemented in Z2PACK [31,32], based on hybrid Wannier functions, to compute the Chern number numerically in the gapped regions for a half-filled spectrum, i.e., $E_F = 0$ in our model. The gap is computed by diagonalization of the tight-binding Hamiltonian for a one-dimensional (1D) chain with z stacking shown in Fig. 1 and zero in-plane momentum.

The electric field breaks the translation symmetry along the z direction, but it does not break the particle-hole symmetry if it has the same impact on all the orbitals. Therefore, the spectrum is still particle-hole symmetric, and the degenerate branches diverge when they acquire a nonzero expectation value $\langle z \rangle$. In fact, the electric field acts as a confining potential on the states due to the Stark effect and tends to close the gap by the coalescence of particle and hole bands with opposite spatial distributions. A simple picture of the band behavior with the electric field can be obtained from perturbation theory. If we consider the term \mathcal{H}_f of Eq. (3) as a perturbation of the Hamiltonian given by Eq. (1), the first-order correction in the energy is

$$\delta E^{(1)} = \langle \psi_{n,\mathbf{k}}^0 | \mathcal{H}_f | \psi_{n,\mathbf{k}}^0 \rangle, \quad (4)$$

where $\psi_{n,\mathbf{k}}^0$ is the unperturbed state of the n th Bloch band. Considering the linear potential given by Eq. (3), the first-order correction is an energy shift proportional to the expectation value z and the electric field:

$$\delta E^{(1)} = ef \langle \psi_{n,\mathbf{k}}^0 | z | \psi_{n,\mathbf{k}}^0 \rangle. \quad (5)$$

Therefore, the states with $\langle z \rangle$ positive (negative) increase (decrease) their energy. Inside the gap, this implies the coalescence of the bands of holes and electrons with opposite signs of $\langle z \rangle$. The bulk states remain almost unchanged, while the energy shift affects especially the states peaked in the interfaces between layers due to their localization.

The topological nature of the bands of this multilayered system is encoded in the band inversion phenomenon occurring between pairs of the conduction and valence bands with different spin polarizations [6]. In fact, even if counterintu-

itive, the spatial localization of the wave functions along the z direction is not a definite signature of the topology of the bands [30] (see Appendix A for more details). In Fig. 3, the states of a $C = 4$ system are plotted in the presence of an electric field of 1 meV/Å. By comparing with the case for zero electric field reported in Fig. 4, it can be noticed that the states that are peaked at the sides of the slab break their inversion symmetry and localize on one of the sides, also lifting the degeneracy between levels. Therefore, within the addition of an electric field, even if the Chern number is still given by the crossing between levels, the localization plays a role because it gives the direction and strength of the displacement of the bands.

Even if the states are modified by the electric field, the main reason for the Chern number tuning is the energy shift given by Eq. (4) and not the spatial localization induced by the field. In fact, the effect of the localization in a single slab of Cr⁻-doped TI is not very relevant as well as the mass renormalization given by the localization (see Appendixes A and B for more details). However, if we consider a slab of finite area in the transverse direction, the topological states appear inside the gap, and they can be identified by their localization in the x - y plane. In Figs. 5 and 6, we show two representative cases of the evolution of the energy as a function of the electric field. In the case plotted in Fig. 5, a $C = 1$ state is turned trivial due to the hybridization of the bands at $f \sim 0.7$ eV/Å, while in Fig. 6, the case of a $C = 2$ going to $C = -1$ is obtained by both the hybridization of the topological bands and by the crossing of a new level coming from the upper part of the energy spectrum.

In the previously mentioned figures, the bands are plotted with the projection of the participation ratio (PR) in the basis of the spatial coordinates, defined as follows:

$$\text{PR} = \frac{(\sum_{i=1}^N p_i)^2}{\sum_{i=1}^N p_i^2}, \quad (6)$$

where N is the number of sites in the system, and p_i is the probability density at site i , i.e., $|\psi_i|^2$. With this definition, the maximum value of PR is N for a completely delocalized

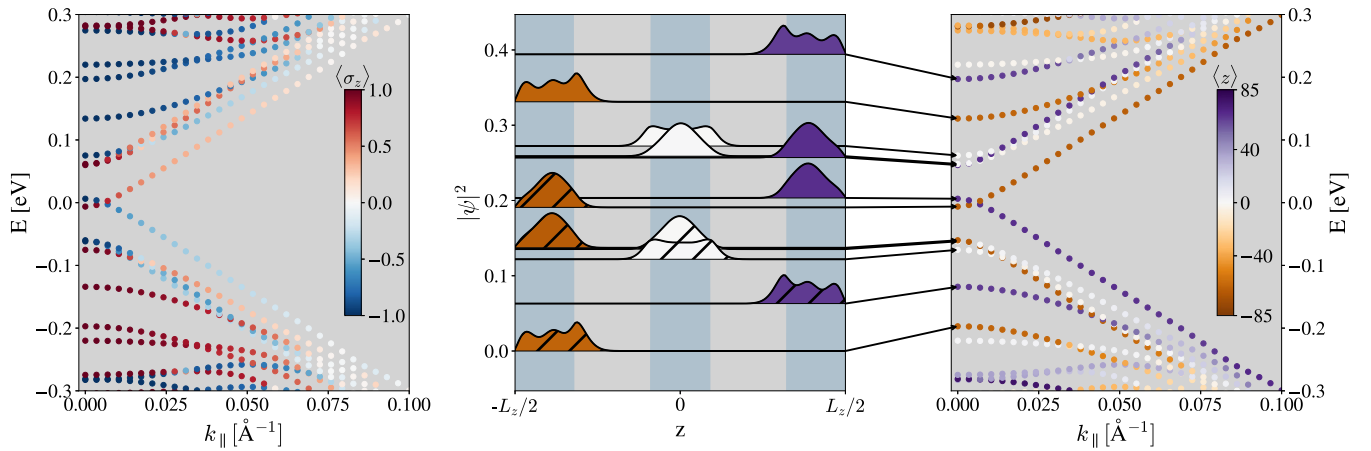


FIG. 3. Energy dispersion and states for a $C = 3$ state at $f = 1 \text{ meV/\AA}$ in a one-dimensional (1D) chain in the z direction. The parameters are $M_0^{\text{Cr}} = -0.2 \text{ eV}$ and $g = 0.32 \text{ eV}$. The energy dispersions show the projection of (a) σ_z and (c) $\langle z \rangle$. (b) Probability density $|\psi|^2$ for the indicated states at $k_{\parallel} = 0$. The states below the Fermi energy are hatched. The parameters correspond to a $C = 4$ state in the absence of an electric field (see Fig. 4 for comparison with the case at $f = 0$).

state and 1 for a state localized in only one site. Although the spatial localization is not a sufficient condition for establishing the topological character of electron states, these states are by their own nature localized in the edges of the sample. Therefore, the PR value is an indicative quantity to track the evolution of the states with the electric field, especially in finite-sized slabs where the states evolve in a continuous way with the electric field, in contrast with the calculated abrupt transitions in the semi-infinite Chern number results represented in Fig. 2.

Finally, we address the problem of measuring these topological phase transitions in a transport setup. An experimentally feasible scenario is a minimal Hall bar with four terminals, where the occurrence of transverse conductance is a key signature of the topological states. Figure 7 shows a schematic view of the setup. The system comprises the multilayered sample connected to four leads with the same stacking of layers. The electric field is applied only in the

scattering region, excluding the leads, and an Anderson-like disorder is added to consider defects and other imperfections of the sample. The Anderson disorder is introduced in the Hamiltonian by adding the following term:

$$\mathcal{H}_A = w(x, y, z) \mathbb{1}_4, \quad (7)$$

where $w(x, y, z)$ is a function that, at each site, gives the onsite random energy, uniformly distributed in the range $[-W/2, W/2]$, with the disorder strength W . The transport simulations have been performed using the package KWANT [33] within the Landauer-Büttiker formalism in a slab of $300 \times 180 \times 170 \text{ \AA}$. The injection energy is set to the Fermi energy with a small positive shift to exceed the finite-sized gap.

Figure 8 shows the conductance for three different sets of parameters as a function of the electric field. The states that contribute to the transverse conductance are mostly the Chern states. Additionally, the hybridized bulk-surface states

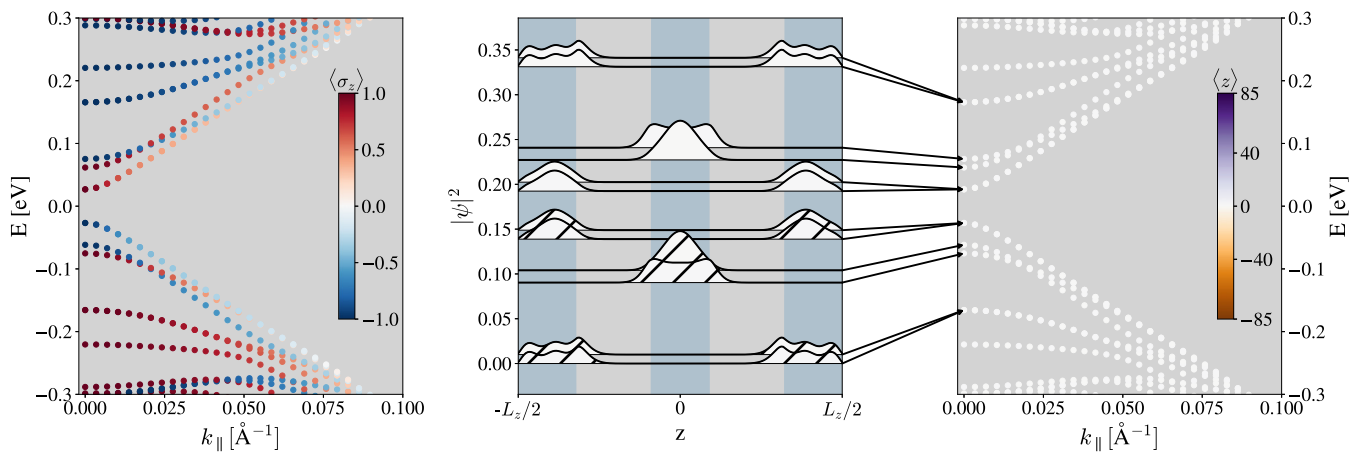


FIG. 4. Energy dispersion and states for a $C = 4$ state in the absence of an electric field. The system is finite only in the z direction, and the parameters are $M_0^{\text{Cr}} = -0.2 \text{ eV}$ and $g = 0.32 \text{ eV}$. The energy dispersions show the projection of (a) σ_z and (b) $\langle z \rangle$. Notice that, due to the symmetry of the structure, the expected value of z is zero for all the states. In (b), the probability density $|\psi|^2$ is plotted for the indicated states at $k_{\parallel} = 0$. The states below the Fermi energy are hatched.

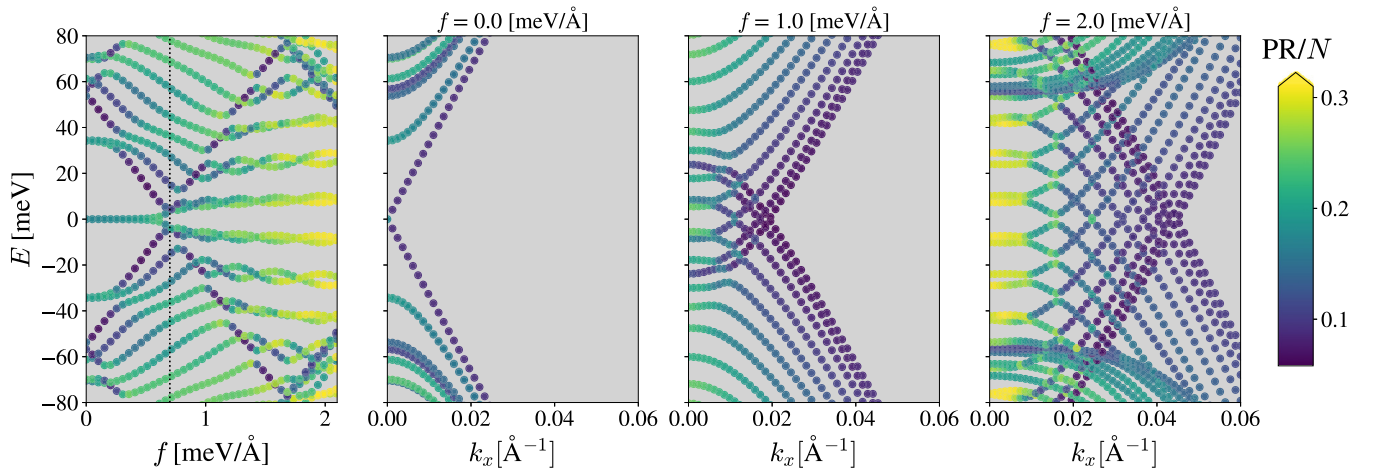


FIG. 5. (a) Energy levels at zero momentum as a function of the electric field and energy dispersion for (b) $f = 0$ meV/Å, (c) $f = 1$ meV/Å, and (d) $f = 2$ meV/Å in a two-dimensional (2D) slab with $L_y = 400$ Å and z stacking corresponding to Fig. 1. The parameters are $M_0^{\text{Cr}} = -0.2$ eV and $g = 0.05$ eV, corresponding to a $C = 1$ in the absence of an electric field, changing to trivial at $f \sim 0.7$ eV/Å; the $f = 0.7$ eV/Å is indicated in a dashed vertical line in (a). The dispersions also show the participation ratio (PR)/ N as an indicator of the localization of the state. The PR is calculated with Eq. (6).

can contribute to the transverse transport as well. Even so, disorder has a significant impact on these trivial states, and their conductance is mostly reduced upon increasing the disorder strength. In the aforementioned figure, the average conductance is plotted together with the squared variance of the disorder realizations for an Anderson disorder with strength $W = 4E_g$, where E_g is the energy of the first mode above the Chern states in the absence of electric field and is a measure of the effective finite-sized gap.

If the transverse conductance is mediated only by Chern states, it must fulfill the following relation:

$$G_{\text{Chern}} = \frac{e^2}{h} \sum_n C(n), \quad (8)$$

where the sum is computed over the Chern numbers $C(n)$ of the occupied bands only, i.e., the states below the Fermi

energy. In Fig. 8, the value of the expected Hall conductance from Eq. (8) is indicated by the crosses. Notice that the average conductance exceeds the expected quantized values due to the contribution of the bulk states that appears at the Fermi energy when the electric field closes the gap. In fact, before the first gap closing, the conductance shows a perfect quantization even in the presence of disorder. At the first gap closing, the conductance starts to decrease smoothly, and the disorder affects the transmission of the trivial states, yielding higher values of the variance.

Due to the breaking of the time-reversal symmetry with the addition of the Zeeman splitting, the current of the anomalous Hall channels flows in a preferential direction. If we use the numbering of leads introduced in Fig. 7 and denote the conductance direction by the order of the subscript indices such that $G_{pq} = G_{p \rightarrow q}$, we get that G_{12} is the preferential current

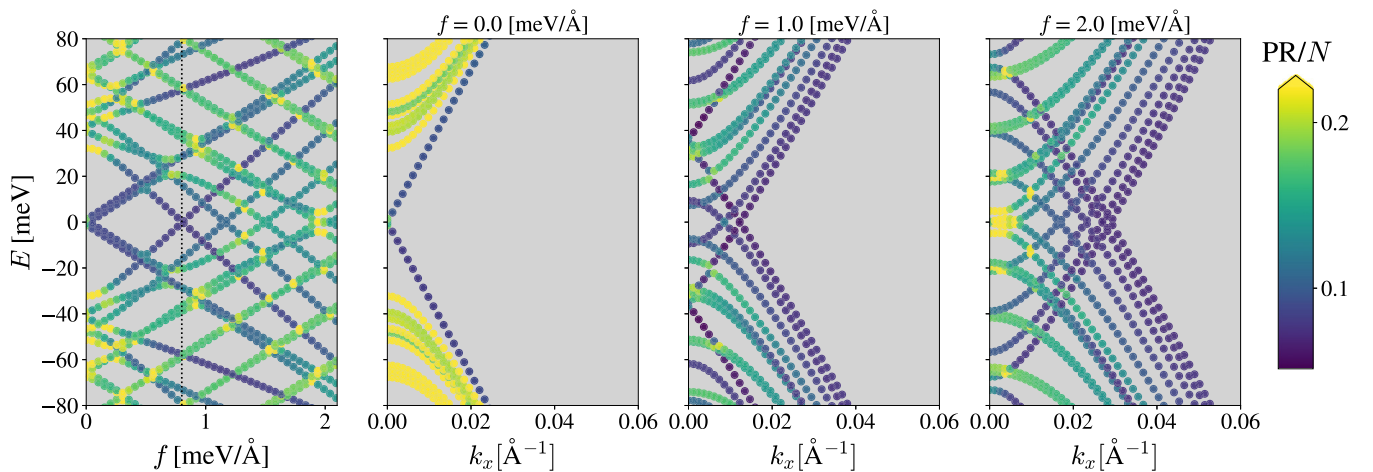


FIG. 6. (a) Energy levels at zero momentum as a function of the electric field and energy dispersion for (b) $f = 0$ meV/Å, (c) $f = 1$ meV/Å, and (d) $f = 2$ meV/Å in a two-dimensional (2D) slab with $L_y = 400$ Å and z stacking corresponding to Fig. 1. The participation ratio (PR) projection is plotted in the scale indicated on the right side of the plots. The parameters are $M_0^{\text{Cr}} = 0.3$ eV and $g = 0.1$ eV, corresponding to a $C = 2$ state that shifts to $C = -1$ at $f \sim 0.8$ eV/Å. The value of $f = 0.8$ eV/Å is indicated in a dashed vertical line in (a).

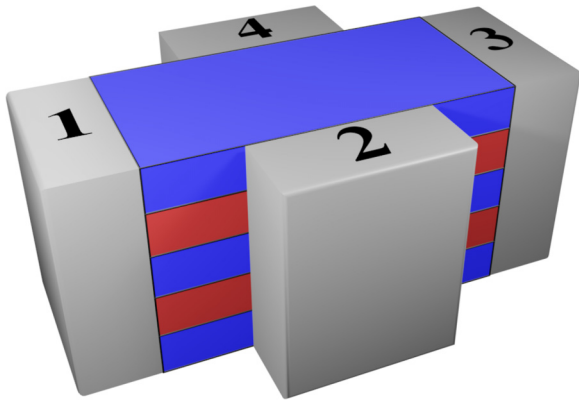


FIG. 7. Sketch of the Hall bar for the conductance simulations. The size is $L_x = 300 \text{ \AA}$ and $L_y = 180 \text{ \AA}$. In the stacking direction (z), the sample resembles the same geometry shown in Fig. 1.

flow direction, while G_{21} is mediated by the contributions of trivial currents.

The measure of the transmission in the opposite direction gives us a criterion to establish the robustness of the topological states with the electric field as well. In Fig. 8, the current in the direct direction is indicated by a solid line, while the reversed current is indicated by a dotted line. Notice that, even if the current in the opposite direction becomes nonzero with the electric field, its value is always reduced in comparison with the G_{12} if there are topological states. In the blue panel in Fig. 8, G_{21} and G_{12} have the same order of magnitude due to the triviality of the phase.

IV. CONCLUSIONS

We have studied the effect of an external electric field on the states of a heterostructure of a magnetically doped TI. The multiple subbands generated by the stacking of alternating Cr^- -doped and undoped layers enable the occurrence of several inverted bands, and by means of this mechanism, multiple Chern states can be achieved. In the presence of an electric field in the stacking direction, the bands coalesce and hybridize, generating new inverted bands and collapsing the previously inverted ones. In this way, the number of Chern states can be tuned externally in the sample, without the need for modifying the number and width of the layers or the doping level. However, due to the multiple band-crossing possibilities, the topological transitions are difficult to predict, and the phase diagrams obtained are complex and intricate. The level of complexity is increased by finite-sized effects in a slab, where the hybridization of edge states located at opposite surfaces is enhanced due to the finite width of the sample.

In all this phenomenology, the general trend is to decrease the number of inverted bands by the collapsing of the topological states. We showed that this effect can be measured in the variation of the transverse conductance as a function of the electric field at constant injection energy at the Fermi level. In our simulations, defects and other imperfections of the device are considered by an Anderson-like model of disorder, which enables a better visualization of the topological features by decreasing the contribution of the trivial bulk states.

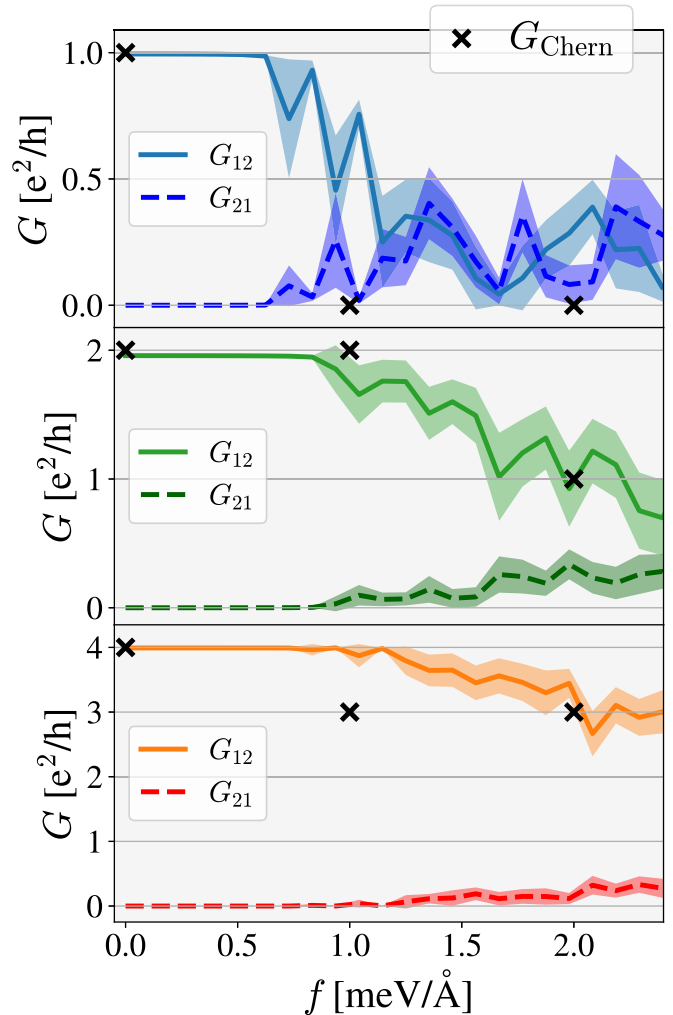


FIG. 8. Conductance as a function of the electric field in a Hall bar with four terminals. Lines indicate the average transverse conductance, while shadowed areas correspond to the squared variance for 100 disorder realizations. Solid lines indicate the conductance G_{12} , while dotted lines are the conductance in the reversed direction G_{21} . Small crosses are the expected values of the transverse conductance given by the Chern number from Eq. (8). The parameters considered correspond to the colored squares in the phase diagram plotted in Fig. 2, given by the following set of parameters: $g = 0.05 \text{ eV}$ and $M_0^{\text{Cr}} = -0.2 \text{ eV}$ (blue), $g = 0.15 \text{ eV}$ and $M_0^{\text{Cr}} = 0.3 \text{ eV}$ (green), and $g = 0.32 \text{ eV}$ and $M_0^{\text{Cr}} = -0.2 \text{ eV}$ (orange).

ACKNOWLEDGMENTS

This paper was supported by the Spanish Ministry of Science and Innovation under Grants No. PID2019-106820RB-C21/22 and No. PGC2018-094180-B-I00 funded by MCIN/AEI/10.13039/501100011033 and FEDER “A way of making Europe.”

APPENDIX A: SPATIAL LOCALIZATION AND EFFECTIVE MODELS

The layers stacked in the z direction exhibit topological states that are peaked typically at the interfaces between them. However, as proved by Wang and Li [30], the spatial

distribution is not evidence of the topology of the bands, which instead is determined by the inversion of their gaps. As already mentioned in Sec. II, in the paper by Wang *et al.* [6], a method of inspection of the effective mass has been proposed and successfully applied to a Cr⁻-doped slab by decoupling the two chiral sectors and Fourier transforming the Hamiltonian. More precisely, the idea is to set the coupling term $B = 0$ and write the Hamiltonian in the basis of $\varphi_n(z) = \sqrt{2/L_z} \sin(n\pi z/L_z + n\pi/2)$, n being an integer. This way, one gets N effective subbands with quantized $k_z = n\pi/L_z$ and effective mass given by

$$m_{\pm}(n) = \langle \varphi_n | M_0(z) | \varphi_n \rangle + M_1(n\pi/L_z)^2 + M_2(k_x^2 + k_y^2) \mp \langle \varphi_n | g(z) | \varphi_n \rangle. \quad (\text{A1})$$

In the case of a single slab of a Cr⁻-doped TI, $M_0(z) = M_0^{\text{Cr}}$ and $g(z) = g$, and both magnitudes have no dependence on the spatial coordinate. Therefore, the effective mass reduces to a function that depends only on the model parameters and the quantized momentum in z : $m_{\pm}(n) = M_0 + M_1(n\pi/L_z)^2 + M_2(k_x^2 + k_y^2) \mp g$. The bands contribute with Chern number $+1$ if $m_+(n) < 0$, -1 if $m_-(n) < 0$, and they are trivial otherwise. The Chern number can be computed by summing up all the contributions by the following expression:

$$C = N_+ - N_-, \quad (\text{A2})$$

where N_{\pm} is the number of bands with $m_{\pm}(n) < 0$. This approximation is valid only for the case of $B = 0$. However, when realistic parameters are added, the phase diagram obtained by this method must be adiabatically modified.

In the case of a multilayered system, the procedure is equivalent, but the expected values in Eq. (A1) depend on the distribution of the Cr⁻-doped layers encoded in the spatial dependence of $M_0(z)$ and $g(z)$. Moreover, due to the dependence on the z coordinate, the mass terms can generate nondiagonal terms in the Hamiltonian in correspondence to different subbands. Therefore, once the mass terms Eq. (A1) are computed, the phase diagram must be adiabatically fitted by the nondiagonal terms and later modified by the term B (see Ref. [30] for more details).

The complexity of the heterostructure makes the approximation of the effective model more complex but still feasible. The electric field generates similar nondiagonal terms, and the effective mode approximation cannot be applied easily. Then the Chern number must be computed numerically by tools such as Z2PACK [31].

In Fig. 9, the expected value of k_z^2 is plotted for the $2N$ bands below the Fermi level in a multilayered system with parameters corresponding to a $C = 4$ state in the absence of an electric field. Notice that the value of k_z^2 decreases by approaching the gap, but it is not modified by the external electric field. The lower panel shows the difference between the expected values in the presence of the electric field and in the pristine case for each band, proving that the modification of $\langle k_z^2 \rangle$ is almost negligible. In conclusion, the change of the effective mass in Eq. (A1) by the varying of momentum does not play a significant role in the modification of the Chern number by the external field.

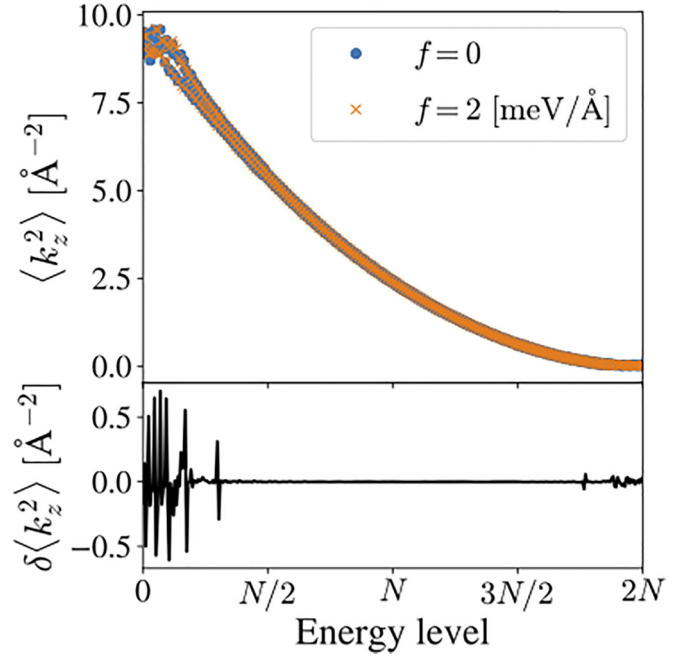


FIG. 9. Expected value of k_z^2 for a multilayered system with parameters $M_0^{\text{Cr}} = -0.2$ eV and $g = 0.32$ eV.

APPENDIX B: EFFECT OF THE ELECTRIC FIELD IN A Cr⁻-DOPED SLAB

In this section, the effect of the electric field on the effective mass is further explored by discussing the case of a Cr⁻-doped slab. The modification of the bands by both the electric field and the Cr⁻ doping in a slab of Bi₂Te₃ and Sb₂Te₃ have already been studied in the literature [24–26]. For comparison with the heterostructure results, we present the phase diagram for a slab of width 30 Å and constant M_0^{Cr} in Fig. 10. Notice that, due to the strong confinement in the z direction, the electric field only shifts slightly the regions of the Chern number in the phase diagram without substantial modifications. If the heterostructure is obtained by the stacking of layers of similar size, we can conclude that the modification of the phase diagram with the applied electric field in Fig. 2 is mostly induced by the crossing of the subbands rather than from the change of the effective Hamiltonian parameters by the electric field.

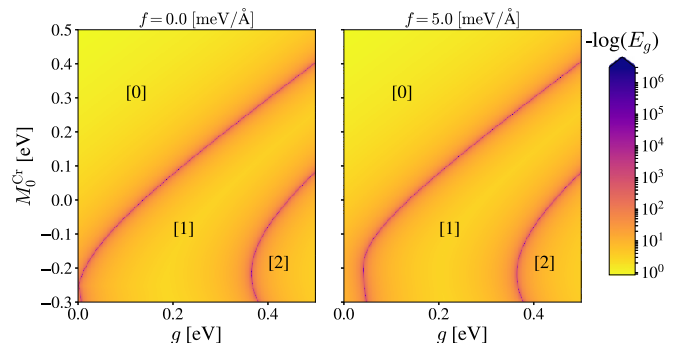


FIG. 10. Phase diagram for a slab of width 30 Å as a function of the mass parameter M_0^{Cr} and the Zeeman splitting g .

- [1] K. von Klitzing, *Annu. Rev. Condens. Matter Phys.* **8**, 13 (2017).
- [2] J. Maciejko, T. L. Hughes, and S.-C. Zhang, *Annu. Rev. Condens. Matter Phys.* **2**, 31 (2011).
- [3] H. Chi and J. S. Moodera, *APL Mater.* **10**, 090903 (2022).
- [4] E. H. Hall, *Am. J. Sci.* **s3-20**, 161 (1880).
- [5] C.-Z. Chang, J. Zhang, X. Feng, J. Shen, Z. Zhang, M. Guo, K. Li, Y. Ou, P. Wei, L.-L. Wang *et al.*, *Science* **340**, 167 (2013).
- [6] J. Wang, B. Lian, H. Zhang, Y. Xu, and S.-C. Zhang, *Phys. Rev. Lett.* **111**, 136801 (2013).
- [7] C. Fang, M. J. Gilbert, and B. A. Bernevig, *Phys. Rev. Lett.* **112**, 046801 (2014).
- [8] Y.-F. Zhao, R. Zhang, R. Mei, L.-J. Zhou, H. Yi, Y.-Q. Zhang, J. Yu, R. Xiao, K. Wang, N. Samarth *et al.*, *Nature (London)* **588**, 419 (2020).
- [9] M. Kim, C. H. Kim, H.-S. Kim, and J. Ihm, *Proc. Natl. Acad. Sci. U.S.A.* **109**, 671 (2012).
- [10] T. Zhang, J. Ha, N. Levy, Y. Kuk, and J. Stroschio, *Phys. Rev. Lett.* **111**, 056803 (2013).
- [11] H. Pan, M. Wu, Y. Liu, and S. A. Yang, *Sci. Rep.* **5**, 14639 (2015).
- [12] J. L. Collins, A. Tadich, W. Wu, L. C. Gomes, J. N. B. Rodrigues, C. Liu, J. Hellerstedt, H. Ryu, S. Tang, S.-K. Mo *et al.*, *Nature (London)* **564**, 390 (2018).
- [13] A. Díaz-Fernández, L. Chico, J. W. González, and F. Domínguez-Adame, *Sci. Rep.* **7**, 8058 (2017).
- [14] A. Díaz-Fernández and F. Domínguez-Adame, *Phys. E* **93**, 230 (2017).
- [15] Y. Baba, A. Díaz-Fernández, E. Díaz, F. Domínguez-Adame, and R. A. Molina, *Phys. Rev. B* **100**, 165105 (2019).
- [16] N. H. Lindner, G. Refael, and V. Galitski, *Nat. Phys.* **7**, 490 (2011).
- [17] J. Cayssol, B. Dóra, F. Simon, and R. Moessner, *Phys. Status Solidi RRL* **7**, 101 (2013).
- [18] G. Usaj, P. M. Perez-Piskunow, L. E. F. Foa Torres, and C. A. Balseiro, *Phys. Rev. B* **90**, 115423 (2014).
- [19] H. Dehghani, T. Oka, and A. Mitra, *Phys. Rev. B* **91**, 155422 (2015).
- [20] C.-K. Chan, P. A. Lee, K. S. Burch, J. H. Han, and Y. Ran, *Phys. Rev. Lett.* **116**, 026805 (2016).
- [21] J. González and R. A. Molina, *Phys. Rev. Lett.* **116**, 156803 (2016).
- [22] J. González and R. A. Molina, *Phys. Rev. B* **96**, 045437 (2017).
- [23] J. W. McIver, B. Schulte, F.-U. Stein, T. Matsuyama, G. Jotzu, G. Meier, and A. Cavalleri, *Nat. Phys.* **16**, 38 (2020).
- [24] Z. Zhang, X. Feng, J. Wang, B. Lian, J. Zhang, C. Chang, M. Guo, Y. Ou, Y. Feng, S.-C. Zhang *et al.*, *Nat. Nanotechnol.* **12**, 953 (2017).
- [25] L. Q. Duong, H. Lin, W.-F. Tsai, and Y. P. Feng, *Phys. Rev. B* **92**, 115205 (2015).
- [26] J. Wang, B. Lian, and S.-C. Zhang, *Phys. Rev. Lett.* **115**, 036805 (2015).
- [27] C.-X. Liu, X.-L. Qi, H. Zhang, X. Dai, Z. Fang, and S.-C. Zhang, *Phys. Rev. B* **82**, 045122 (2010).
- [28] R. Yu, W. Zhang, H.-J. Zhang, S.-C. Zhang, X. Dai, and Z. Fang, *Science* **329**, 61 (2010).
- [29] J. Zhang, C.-Z. Chang, P. Tang, Z. Zhang, X. Feng, K. Li, L. I. Wang, X. Chen, C. Liu, W. Duan *et al.*, *Science* **339**, 1582 (2013).
- [30] Y.-X. Wang and F. Li, *Phys. Rev. B* **104**, 035202 (2021).
- [31] D. Gresch, G. Autès, O. V. Yazyev, M. Troyer, D. Vanderbilt, B. A. Bernevig, and A. A. Soluyanov, *Phys. Rev. B* **95**, 075146 (2017).
- [32] A. A. Soluyanov and D. Vanderbilt, *Phys. Rev. B* **83**, 235401 (2011).
- [33] C. W. Groth, M. Wimmer, A. R. Akhmerov, and X. Waintal, *New J. Phys.* **16**, 063065 (2014).